Structure and hydrogen sorption properties of Mg-Mg2Ni nanoparticles prepared by gas phase condensation

Structure and hydrogen sorption properties of Mg-Mg_2Ni nanoparticles prepared by gas phase condensation

Raffaello Mazzaro,[1,2] Luca Pasquini[1,2]

1-Department of Physics and Astronomy, University of Bologna, v.le Berti-Pichat 6/2, 40127 Bologna, Italy

2-Unit of Bologna, Institute for Microelectronics and Microsystems, National Research Council, via Gobetti 101, 40129, Bologna, Italy

Abstract. The aim of this work is to investigate the hydrogen sorption kinetics and thermodynamics of Mg-Ni nanoparticles at relatively low temperature in relation to their microstructure. To this purpose, Mg-Ni nanoparticles (20 at.% Ni) were prepared by gas phase condensation employing two thermal vapour sources. In the as-prepared state, Mg and Ni are mixed within individual nanoparticles, but the intermetallic Mg_2Ni compound is not detected. After keeping the nanoparticles at 150 °C for two hours under high vacuum or at a mild hydrogen pressure of 0.15 bar, the formation of a Mg-Mg_2Ni or MgH_2-$Mg_2NiH_{0.3}$ nanocomposite is observed. Subsequently, fast kinetics of hydrogen sorption are recorded at 150 °C with activation energy of 80 ± 8 kJ/mol (absorption) and 60 ± 6 kJ/mol (desorption). However, the maximum hydrogen storage capacity is limited to 2.5 wt% because the transformation from $Mg_2NiH_{0.3}$ to Mg_2NiH_4 does not take place at 150 °C even at pressures well above the expected thermodynamic equilibrium. Therefore, only the transformation Mg↔MgH_2 contributes to the reversible storage capacity. The corresponding equilibrium pressure determined by pressure-composition isotherms of absorption and desorption at 150 °C is 7.5 mbar, very close to the extrapolated value for bulk Mg. The partial replacement of Ni with Fe does not significantly alter the thermodynamics and kinetics of hydrogen sorption. The structure and hydrogen sorption properties of Mg-Ni NPs are compared to those of Mg-Ti NPs prepared by a similar procedure.

Keywords: Hydrogen storage; Nanoparticle; Magnesium; Nickel; Gas Phase Condensation; Intermetallic

Introduction

The large-scale production of green hydrogen from renewable sources is considered one key ingredient of the transition towards a carbon-neutral society. In this scenario, hydrogen storage solutions that satisfy the requirements of safety, low-footprint, economic viability, and social acceptance will be as important as abating the costs of green hydrogen production and developing the relevant infrastructure for hydrogen distribution. Hydrogen storage in metallic alloys, which exploits the reversible metal-to-hydride transformation tuneable by pressure and temperature, offers high volumetric density, intrinsic safety, and long term stability, and as such is a suitable option both for short-term and seasonal storage on a wide scale range [1].

Magnesium (Mg) and Mg-based alloys are notoriously among the most interesting and studied hydrogen storage materials [2–4]. In fact, Mg can store up to 7.6 wt% hydrogen in the form of MgH_2, it is abundant in the Earth's crust, and has the potential to be produced at low cost [5]. The most frequently cited problems related to the use of Mg-based hydrides are the high stability, quantified by the formation enthalpy $\Delta H = -74$ kJ/molH_2 [2], and the sluggish kinetics; the typical activation energy is $95 - 130$ kJ/mol (absorption) and $120 - 160$ kJ/mol (desorption), respectively [6,7]. High stability implies that H_2 desorption at 1 bar takes place at $T \gtrsim 285$°C; this equilibrium thermodynamic condition is rather difficult to circumvent. On the other hand, spectacular improvements of the hydrogen sorption kinetics have been obtained by a combination of nanostructuring and addition of catalysts [8–10], bringing the activation energy in the range of 50-70 kJ/mol for both absorption and desorption.

Even though thermodynamic stability represents a barrier to hydrogen release at near-ambient conditions, as required to feed a proton exchange membrane fuel cell, it turns advantageous for implementing hydrogen absorption at low pressure $p(\mathrm{H}_2)$, provided the kinetics are fast enough. Therefore, Mg-based alloys are good candidates for matching those applications, in which H_2 is produced at low-pressure, e.g. in photoelectrochemical water splitting devices [11]. The conditions for subsequent H_2 release,

though non-ideal, are much milder than for hydrogen getter alloys and may be brought closer to industrial use by a knowledge-based abatement of the kinetic barriers that hinder H_2 desorption at low temperature. For instance, MgH_2-TiH_2 composite nanoparticles can reversibly store ≈ 4 wt% hydrogen in the $100 - 150$ °C range at a mild $p(\mathrm{H}_2) \approx 0.1$ bar for absorption and a few mbar for desorption [12,13], which is very close to the thermodynamic threshold, by virtue of very low activation energies.

Among the Mg-based alloys and compounds, Mg-Ni alloys have been raising particular interest [14]. In fact, while Mg and Ni are mutually immiscible, their line compound Mg_2Ni has the ability to form the complex Mg_2NiH_4 hydride with 3.6 wt% gravimetric storage capacity. Moreover, the presence of Ni confers the ability to split and recombine H_2. Therefore, Mg-Ni alloys with Ni content ≤ 33 at.% prepared using different methods have been studied to determine the Ni content and microstructure that optimize sorption kinetics without losing too much capacity compared to pure Mg. The ternary Mg-Ni-H phase diagram has been assessed from experimental data [15]: by increasing $p(\mathrm{H}_2)$ at constant temperature, a metallic Mg-Mg_2Ni composite sequentially transforms into Mg - $Mg_2NiH_{0.3}$ (the latter being a solid solution of H in Mg_2Ni), then into MgH_2 - $Mg_2NiH_{0.3}$, and finally into MgH_2 - Mg_2NiH_4. The formation of Mg_2NiH_4 at higher pressure than MgH_2 indicates that Mg_2NiH_4 is less stable than MgH_2 , and in fact it has a less negative formation enthalpy of -64 kJ/mol H_2 [16].

The synthesis and processing routes employed for the preparation of Mg-Ni alloys are numerous. Ball milling [17–19] and severe plastic deformation (SPD) techniques such as equal-channel angular pressing (ECAP) [20,21] and high pressure torsion (HPT) produce alloys with a fine-grained microstructure either in powder form or as compact specimens. The two techniques have also been combined in the compaction of ball-milled powders by HPT [22,23]. Forging of compacts made of Mg and Ni powders can also produce specimens having microstructures with good hydrogen sorption properties [24]. In particular, forging above 400 °C led to the formation of Mg_2Ni intermetallic via solid-state reaction, while no phase transformation occurred upon cold forging [24]. Induction melting and casting was employed to produce near-eutectic Mg-Mg_2Ni composites with good cycling properties [25]. Rapid solidification via melt-spinning of a Mg-10Ni-2Mm alloy (Mm=Lanthanum-rich Mischmetal) yielded a nanoscale microstructure with semi-coherent interfaces and improved hydrogen sorption properties thanks to fast diffusion [26].

In addition, several techniques have been developed for the preparation of Mg-Ni nanoparticles (NPs). The reduction of Mg and Ni in a liquid solvent was exploited to obtain Ni-doped Mg NPs wrapped by reduced graphene oxide (rGO) [27], which exhibit a storage capacity of 6.5 wt% while maintaining robustness. The reaction of Mg vapours with pre-formed Ni NPs on the surface of graphene sheets was used to prepare Mg_2NiH_4 single crystal NPs encapsulated in a MgO layer that showed very low activation energy and fast kinetics for hydrogen desorption [28]. Mg_2Ni intermetallic NPs were synthesized by annealing a mixture of Mg and Ni NPs grown by hydrogen plasma-metal reaction [29]. Mg-Ni NPs nanoconfined in templated carbon were synthesized by a three-step procedure consisting of i) Ni NPs loading by incipient wetness, ii) synthesis of MgH_2 NPs via impregnation with an organometallic precursor, and iii) annealing at suitable temperature/hydrogen pressure [30].

The Mg-Ni alloys and NPs referenced above can exhibit storage capacity in the $5 - 6$ wt% range with desorption times in the order of $5 - 10$ minutes at 300 °C [20,21]. However, experimental studies of the hydrogen sorption properties (both kinetics and thermodynamics) in the low temperature range (100-150 °C) are scarce, mainly because of kinetic limitations: we intend to fill this the gap with the present work. To this purpose, we prepare Mg-Ni bi-elemental NPs by gas phase condensation of mixed Mg and Ni vapours, following a similar approach to that adopted for Mg-Ti NPs [12,13]. Upon exposure to hydrogen at 150 °C and $p(\mathrm{H}_2) \approx 0.15$ bar, a nanoscale two-phase mixture of MgH_2 and $Mg_2NiH_{0.3}$ is obtained. We determined the kinetics of hydrogen absorption and desorption, the corresponding activation energies, and the plateau pressures at 150 °C by means of an *in situ* set up attached to the ultra-high vacuum chamber for NPs growth. In this article, we also draw a comparison between Mg-Ni and benchmark Mg-Ti NPs, discussing the principal reasons for their different behaviour, and examine the effect of partially replacing Ni with Fe.

Experimental

Mg-Ni nanoparticles were prepared by gas phase condensation following a procedure previously reported for Mg-Ti NPs [12,13]. Briefly, Mg and Ni are evaporated in Joule-heated tungsten boats separated by about 2 cm inside a ultra-high vacuum (UHV) chamber previously evacuated to $5 \cdot 10^{-8}$ mbar. During evaporation, an equimolar mixture of He and H_2 was admitted into the chamber in correspondence of the boats at a flow rate of 10 scc/min. In this situation, the pressure within the evaporation chamber was dynamically maintained at 2.6 mbar. The metallic vapours quickly become supersaturated due to collisions with the ambient gas, leading to the nucleation of NPs that are transported by both the imposed gas flow and natural convection toward a liquid nitrogen-cooled cylindrical collector where they deposit by thermophoresis. Finally, the NPs were scraped-off the collector under high vacuum and transferred into a glass ampoule in a secondary UHV chamber. The typical amount of NPs prepared in this way was about 50 mg in 30 minutes of evaporation. The transition from this laboratory quantity to a significantly larger amount can be achieved in principle by increasing the size of the crucibles and implementing continuous operation with more efficient collection of the nanopowders. As discussed in a recent review, vapour-phase synthesis is compatible with scalability for large-scale production of NPs [31].

The heating powers supplied to the thermal sources were tuned in order to obtain a Ni content, defined as Ni/(Ni+Mg), of about 20 at.%. Although a fine stoichiometry control is not possible with this method, a good reproducibility can be achieved after a suitable calibration if all experimental conditions are carefully monitored. The actual composition of the NPs was determined *a posteriori* with a Leica Cambridge Stereoscan 360 scanning electron microscope equipped with an Oxford Instruments X-ray detector for energy dispersive X-ray microanalysis.

The hydrogen sorption properties were measured *in situ* in the secondary chamber using an analog capacitive pressure sensor (Varian, range < 1 bar, output 0-10 Volt), the output of which was digitalized by a 16-bit Digital-To-Analog Converter (National Instruments myDAQ). In the pressure range < 0.2 bar, the analog signal was amplified 5 times before digitalization. The nominal resolution of the measurement chain is about 6×10^{-3} mbar in the range < 0.2 bar, where almost all measurements were performed, and 3×10^{-2} mbar above. The point-to-point oscillations were reduced to less than 4×10^{-3} mbar by performing continuous data acquisition at 1000 Hz and averaging over a buffer of 100 data points.

The temperature was controlled using a resistive heater wrapped outside the sample holder, a K-type thermocouple, and a variable power supply controlled by a feedback loop. The temperature accuracy and stability were about ± 0.5 °C, yielding an overall temperature uncertainty of ± 1 °C. The first treatment always consisted in a hydrogenation procedure, in which $p(\mathrm{H_2})$ was set to 0.15 bar at room temperature, followed by heating up to 150 °C. After 2 hours at 150 °C, the sorption kinetics were measured in static conditions by recording the pressure change after setting a given hydrogen pressure $p(\mathrm{H_2})$. In particular, desorption kinetics were typically measured starting from high vacuum. Pressure-composition isotherms (PCI) at 150 °C were recorded in quasi-equilibrium conditions by monitoring the $p(\mathrm{H_2})$ change for 1000 s after each increment (absorption) or decrement (desorption). The amount of absorbed or released hydrogen was determined by calibrating the chamber volume (≈ 5 litres). As a reference for the reader, a pressure change of 1 mbar corresponds to a H_2 mass of about 0.43 mg. The purity of the H_2 gas used in the experiment was 99.995%. The last step of the characterization was always an absorption at 150 °C and $p(\mathrm{H_2}) = 0.15$ bar. After that, the sample holder was cooled to room temperature and filled with pure Argon at atmospheric pressure. The sample vial was then sealed under Ar for further analyses.

Microstructural and nanoscale compositional analyses were carried out with a Philips TECNAI F20 ST transmission electron microscope (TEM) operating at 120 kV. The instrument is equipped with dispersion micro-analysis of energy (EDS) and scanning transmission (STEM) accessory. High-resolution TEM (HR-TEM) images were taken in the phase contrast mode. STEM images were recorded using a High Angle Annular Dark Field (HAADF) detector. For TEM observations, a sealed vial containing the NPs was filled with isopropyl alcohol using a syringe that perforated the plastic cap. The obtained suspension was sonicated, and few drops of the suspension were casted on a copper grid coated with an amorphous carbon film. The NPs were shortly exposed to ambient air prior to insertion into the microscope chamber.

X-ray Diffraction (XRD) profiles were collected under ambient air using a PANalytical X'celerator diffractometer equipped with a solid-state multi-element detector. The instrument was operated in

parafocusing Bragg-Brentano geometry with a 2θ angular step of 0.016° and an effective counting time $>$ 100 s per point. Ni-filtered Cu K_α radiation without monochromator was employed. The incoming X-ray beam was collimated by divergence and anti-scatter slits with an aperture of 0.5°. The lattice parameters and crystallite size of the various phases were determined with the MAUD full-profile refinement software [32].

Results and Discussion

Structure and morphology of Mg-Ni nanoparticles

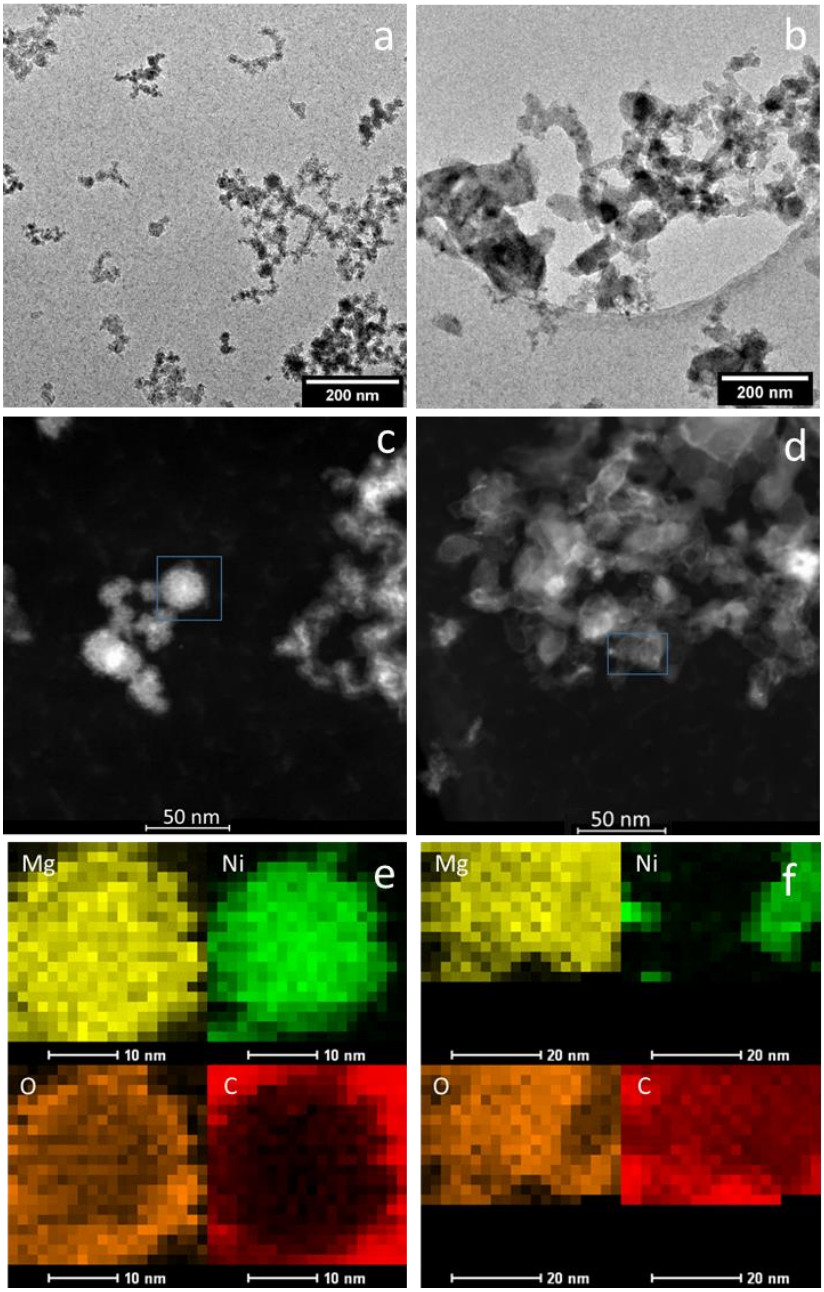

Figure 1. Morphological and composition analysis of Mg-Ni NPs (20 at.% Ni) both as-prepared (left column) and after ten hydrogen sorption cycles ending in the hydride state (right column). (a,b) bright field TEM images; (c,d) STEM-HAADF images; (e,f) STEM-EDX compositional maps of selected areas in (c,d). The C map is also reported to help visualization of Mg-Ni NPs, in contrast to the supporting amorphous carbon film.

Figure 1 shows the morphology and elemental distribution of Mg-Ni NPs (20 at.% Ni) in the as-prepared condition (left column) and after ten hydrogen sorption cycles at 150 °C (right column). In the as-prepared state, the Mg-Ni NPs form aggregates with an irregular shape and an aggregate size that easily exceeds 100

nm, as typical of the gas-phase condensation method (Figure 1a) [33]. The size of the individual NPs within the aggregates is significantly smaller, showing a distribution between 10 and 40 nm with an average value around 25 nm and a nearly spherical shape (Figure 1c). It is interesting to remark that gas-phase condensation of pure Mg typically yields much larger individual NPs (> 100 nm) with a polyhedral shape that reflects the hcp structure of Mg [34]. In the present case, the simultaneous co-evaporation of Ni from and adjacent crucible apparently inhibits the coalescence and recrystallization of the primary Mg NPs that form by homogeneous nucleation in the gas phase, thus resulting in smaller individual Mg-Ni NPs. This effect has already been reported for the gas-phase condensation of Mg-Ti NPs under similar conditions [35,36]. The transition metal (TM) evaporated from the second source along the gas flow is incorporated within the incoming Mg NPs and act as grain refiner, impeding the coalescence that would normally occur for pure Mg NPs. It remains to be ascertained whether the TM is atomically dissolved or in the form of ultrafine crystallites within the Mg matrix, or both. In both cases, gas phase condensation using Mg and TM sources brings two simultaneous benefits, i.e. the refinement of the Mg NPs size distribution and the addition of a catalyst that can favour the dissociation and recombination of H_2 at the NPs surface.

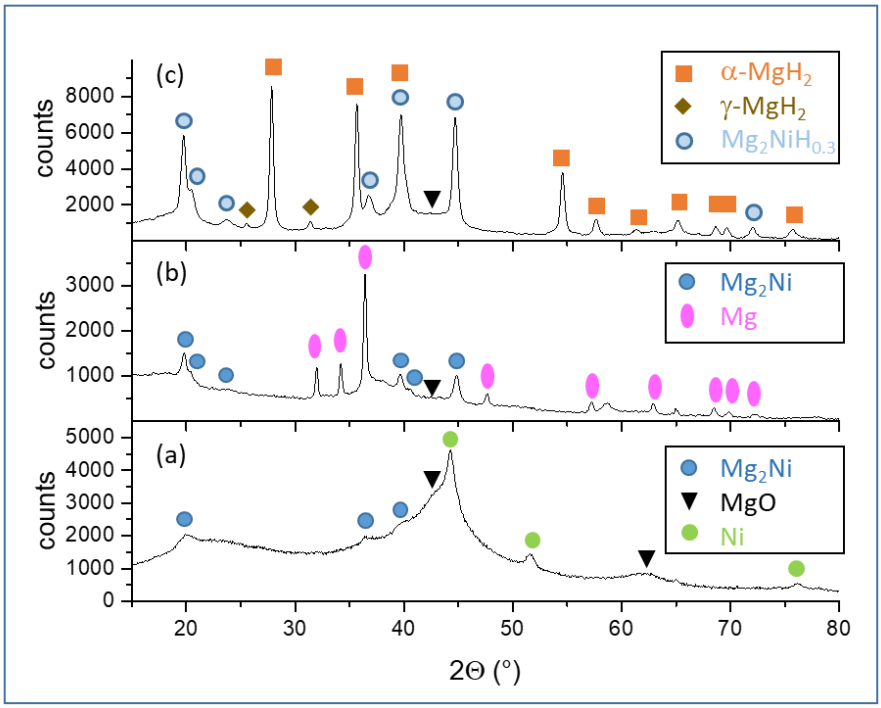

Figure 2. XRD profiles of Mg-Ni NPs (20 at.% Ni) under different conditions. (a) as-prepared; (b) after a heat treatment of 2 hours in vacuum at 150 °C; (c) after ten hydrogen sorption cycles at 150 °C ending in the hydride state. The main Bragg peaks of the crystalline phases detected in the profiles are marked and labelled. Measurements were carried out in air at ambient conditions.

The mixing of Mg and Ni within individual as-prepared NPs is confirmed by the STEM-EDX elemental maps reported in Figure 1e. The core contains both Mg and Ni, while the NP surface shell displays little or no Ni content and appears enriched in Mg and O. This core@shell morphology, where the core contains both Mg and Ni while the shell is constituted of MgO, develops when the Mg-Ni NPs are exposed to air due to the higher enthalpy of oxidation of Mg compared to Ni. In fact, as-prepared Mg-Ni NPs are extremely air-sensitive, as shown by the XRD profile in Figure 2a. Here, no traces of metallic hcp Mg are detected, while two broad peaks due to MgO are visible at about 43.0° and 62.3° (black triangles). The pattern in Figure 2a also shows the Bragg reflections of fcc Ni (green circles) as well as weak peaks (blue circles) that match reasonably well the most intense Bragg reflections expected for hexagonal Mg_2Ni (JCPDS:35-1225; Space Group $P6_222$; $a = 5.210$ Å; $c = 13.230$ Å). Moreover, a broad hump centred at about 23° may indicate the presence of an amorphous Mg-Ni phase [14]. Altogether, these results indicate that gas phase condensation with two vapour sources leads to nanoscale mixing of Mg and Ni but only to partial Mg-Ni alloying. Clearly,

an accurate study of the as-prepared structure and morphology would require fully inert extraction and handling of the Mg-Ni NPs (including insertion into the TEM), which is not easy to implement and not available in the present investigation. Nevertheless, STEM-EDX analysis confirms the effectiveness of gas-phase condensation in the synthesis of bi-elemental NPs.

The Mg-Ni phase diagram predicts a coexistence of Mg and Mg_2Ni for the 20 at.% Ni content examined in this study. Therefore, the fine mixing of Mg and Ni is a perfect start for obtaining a Mg-Mg_2Ni nanocomposite by means of a mild thermal treatment. In fact, after a heat treatment of 2 hours at 150 °C under high vacuum, the XRD profile of Mg-Ni NPs (Figure 2b and Table I) clearly shows the Bragg reflections of both hcp Mg and hexagonal Mg_2Ni. It is worth noticing that the formation of Mg_2Ni starting from a physical mixture of pure Mg and Ni NPs, as studied by Shao et al [29], required annealing at much higher temperatures of about 350 °C under 40 bar hydrogen pressure followed by dehydriding. This difference confirms that Mg and Ni are already well mixed in the as-prepared state, requiring only short-range diffusion to reorganize the atoms in the equilibrium crystalline phases Mg and Mg_2Ni.

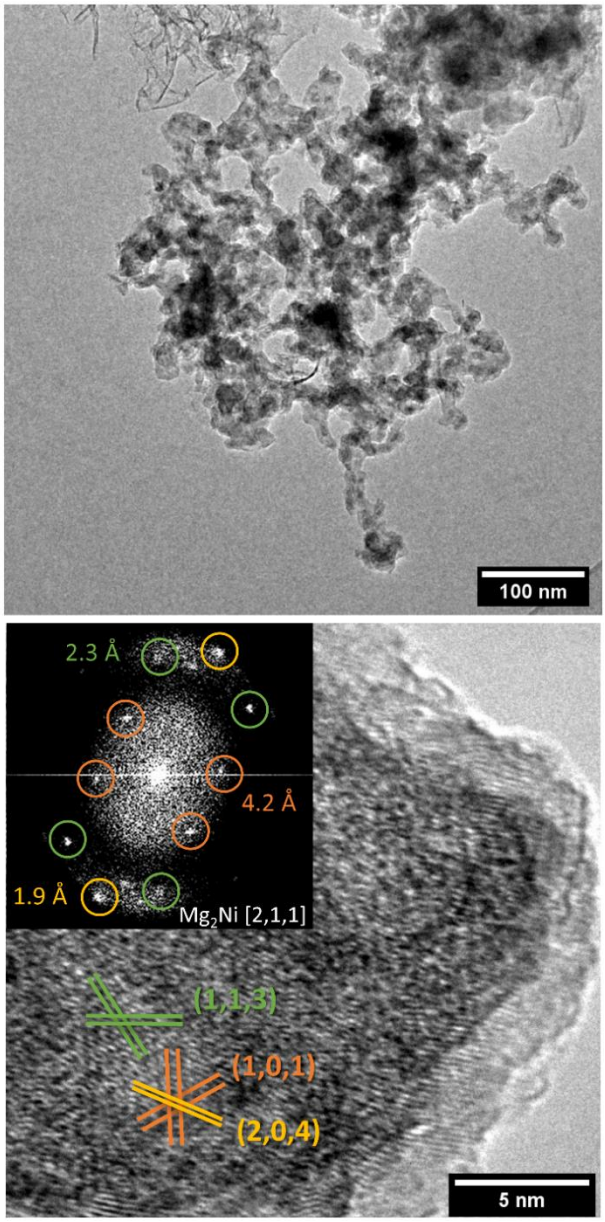

Figure 3. (a) Bright-field TEM and (b) HRTEM of Mg-Ni NPs (20 at.% Ni) subjected to a heat treatment at 150 °C for 2 hours in high vacuum. The FFT pattern shown in the top left inset of (b) shows the reflections for the Mg_2Ni phase on the [211] zone axis; the corresponding lattice planes are highlighted in the HRTEM image using the same colours.

After the treatment at 150 °C, the NPs exhibit a higher degree of aggregation, as shown by Figure 3a. The formation of the intermetallic compound Mg_2Ni is confirmed by the HRTEM analysis reported in Figure 3b. The lattice planes highlighted in the HRTEM image correspond to the reflections for the Mg_2Ni phase on the [211] zone axis, shown in the FFT pattern along with the respective interplanar distance. The lighter envelope visible around the Mg_2Ni phase in Figure 3b is again an MgO shell. However, the humps related to MgO in the XRD profile are much lower than those of Mg and Mg_2Ni, indicating that the heat-treated NPs are much less air-sensitive than the as-prepared ones. This difference may be due to the lowering of the surface area, and hence reactivity, that accompanies the aggregation of the NPs during the treatment.

The morphology and structure of Mg-Ni NPs further evolve upon repeated hydrogen sorption cycles. Figure 1b, which refers to a sample after ten cycles at 150 °C ending in the hydride state, highlights the presence of many high-density aggregates that were completely absent in the as-prepared condition. As shown in the STEM-HAADF image (Figure 1d) for the same sample, the individual initial NPs within aggregates can no longer be identified, indicating that interdiffusion of Mg and Ni, as well as surface diffusion driven by capillary forces, significantly reshapes the morphology of the system. The STEM-EDX elemental maps in Figure 1f show regions containing only Mg (without Ni) separated by mixed Mg-Ni regions; it is straightforward to assign the former to Mg or MgH_2 and the latter to Mg_2Ni or $Mg_2NiH_{0.3}$ (see discussion below). The NPs surface is still contaminated by MgO due to air exposure; moreover, MgH_2 dissociates and the MgO content increases during prolonged observation under the electron beam [37], which justifies the strong O signal in former MgH_2 domains. The increase of MgO is likely due to the reaction of Mg metal with residual oxygen or water either present in the TEM column or physically adsorbed on the NPs surface. The typical size of the phase domains lies in the tens of nm range.

The XRD profile of hydrogen-cycled NPs, reported in Figure 2c, permits to identify the main crystalline phases as tetragonal rutile-type α-MgH_2 (JCPDS: 72-1678; Space Group $P4_2/mnm$; $a = 4.5025$ Å; $c = 3.0123$ Å) and hexagonal $Mg_2NiH_{0.3}$ (JCPDS: 43-0988; Space Group $P6_222$; $a = 5.2315$ Å; $c = 13.404$ Å). In addition, a small amount of the orthorhombic polymorph γ-MgH_2 (Space Group $Pbcn$; $a = 4.5051$ Å; $b = 5.4197$ Å; $c = 4.9168$ Å), along with broad humps due to MgO, are visible. The presence of γ-MgH_2, usually observed in ball-milled MgH_2 due to severe plastic deformation, may be induced by strains that develop at the interface between MgH_2 and $Mg_2NiH_{0.3}$ because of the large volume expansion associated with the Mg-MgH_2 transformation. The formation of γ-MgH_2 after the first hydriding was reported also for Mg-Ti NPs [13,36]; therefore, it seems a common feature of biphasic nanomaterials linked with nanoscale mixing of two phases, only one of which undergoes a large volume change at the given $p(\mathrm{H_2}), T$ conditions.

The best-fit parameters obtained from the Rietveld analysis are reported in Table I. Notice that an XRD profile very similar to Figure 1c was recorded after the first hydrogen absorption, as shown by the comparison in Figure S1 of the Supplementary Information. This demonstrates that full transformation from Mg into MgH_2 takes place in less than two hours at 150 °C and $p(\mathrm{H_2}) = 0.15$ bar without activation. The most relevant cycling-induced change is the decreased abundance of the γ-MgH_2 phase (Figure S1 and Table I), which is not surprising given the metastability of the orthorhombic polymorph at ambient pressure. Notably, at the low cycling temperature of the present study γ-MgH_2 is more persistent than typically observed at about 300 °C, where it disappears very rapidly. This observation agrees with a recent study that demonstrated a much higher stability of γ-MgH_2 when annealed in H_2 atmosphere at 250 °C compared to 300 °C [38].

The transition from Mg_2Ni to $Mg_2NiH_{0.3}$ due to hydrogen absorption is pointed out by the shift of the Bragg reflections to lower angles. In fact, $Mg_2NiH_{0.3}$ and Mg_2Ni share the same space group and positions of the Mg and Ni atoms; therefore, their XRD patterns are not easy to distinguish, especially for nanocrystalline samples. However, the unit cell volume of $Mg_2NiH_{0.3}$ is about 2 % larger because of the lattice expansion that accompanies the incorporation of hydrogen. This difference is clearly revealed by the increase of the lattice parameters detected by Rietveld full-profile analysis, the results of which are reported in Table I and Figure S2 for the main crystalline phases observed after the various treatments at 150 °C, i.e. simple heating under vacuum, first hydride formation, and hydrogen cycling. Moreover, the absorption of H by Mg_2Ni leading to the formation of $Mg_2NiH_{0.3}$ is supported by the PCI measurements described in the next section.

Table I: Lattice parameters, crystallite size d, and relative abundance of crystalline phases detected in XRD profiles, as determined by Rietveld analysis. The results are given for Mg-Ni NPs subjected to the following treatments at 150 °C: (I) two hours under high vacuum; (II) two hours at $p(\mathrm{H}_2) = 0.15$ bar; (III) as (II) followed by ten complete hydrogen sorption cycles. $Mg_2NiH_{0.x}$ actually corresponds to Mg_2Ni in (I) and to $Mg_2NiH_{0.3}$ in (II) and (III). The numbers within parenthesis represent the standard deviations in units of the last digit. The R_w factors obtained from the fit are 4.4, 2.7, and 3.3 % for I, I, and III respectively.

	Mg				$Mg_2NiH_{0.x}$				α-MgH_2				γ-MgH_2				
	a(Å)	c(Å)	d(nm)	wt%	a(Å)	c(Å)	d(nm	wt%	a(Å)	c(Å)	d(nm)	wt%	a(Å)	b(Å)	c(Å)	d(nm)	wt%
I	3.212(1)	5.215(1)	80(8)	38(4)	5.213(1)	13.306(5)	21(2)	62(6)	--	--	--	--	--	--	--	--	--
II	--	--	--	--	5.231(1)	13.502(4)	20 (2)	63(6)	4.524(1)	3.020(1)	31(3)	33(3)	4.520(5)	5.446(5)	4.955(5)	24(2)	6(1)
III	--	--	--	--	5.236(1)	13.455(2)	27(3)	64(6)	4.527(1)	3.023(3)	44(4)	34(4)	4.51(1)	5.45(1)	4.95(1)	24(3)	2.0(2)

The crystallite size of both α-MgH_2 and $Mg_2NiH_{0.3}$ increase with hydrogen cycling while the lattice parameters remain constant and in agreement with the reference values. Heating under vacuum leads to a Mg crystallite size of about 80 nm, much larger than the initial NPs diameter and the α-MgH_2 crystallite size of 27 nm obtained by heating under hydrogen. This suggests that coarsening is more severe for metallic Mg than for MgH_2, and that it is convenient to perform the first heating treatment under hydrogen, as we did before measuring the hydrogen sorption properties.

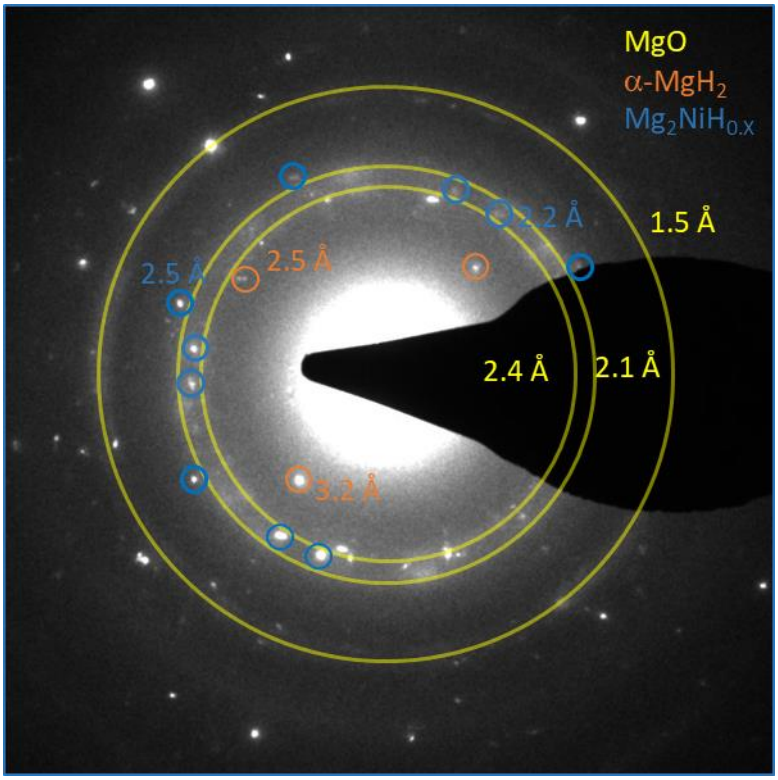

Figure 4. SAED pattern taken on the Mg-Ni NPs (20 at.% Ni) subjected to ten hydrogen sorption cycles ending in the hydride state. The diffraction spots and interplanar spacing that correspond to the reflections of α-MgH_2 and Mg_2Ni (or $Mg_2NiH_{0.3}$) phases are highlighted. The yellow rings correspond to MgO, the amount of which increases during electron beam-induced decomposition of MgH_2. $Mg_2NiH_{0.x}$ stands for either Mg_2Ni or $Mg_2NiH_{0.3}$ because the resolution does not allow distinguishing the tiny difference in interplanar spacing.

The selected area electron diffraction (SAED) pattern in Figure 4, taken on a sample after ten hydrogen sorption cycles ending in the hydride state (same sample of Figure 2c), shows bright spots that can be attributed to α-MgH_2 and Mg_2Ni (or $Mg_2NiH_{0.3}$), thus confirming the above picture. As already noted, TEM observation of MgH_2 is notoriously difficult because it quickly decomposes under electron irradiation in high vacuum [37]. Therefore, the SAED in Figure 4 was taken on a large area before carrying out any other TEM

analysis in order to minimize the irradiation. The diffuse rings in the SAED belong to MgO, which occurs in the form of very fine crystallites (2-3 nm) principally located in the shell of the NPs, in agreement with previous reports [34,39].

Finally, we notice that, although the transformation of Mg_2Ni into the complex Mg_2NiH_4 hydride is expected at the temperature and pressure conditions used for the hydrogen sorption cycles, the Bragg reflections of Mg_2NiH_4 are not visible in Figure 2c. The obtained structural picture, indicating the coexistence of nanoscale domains of MgH_2 and $Mg_2NiH_{0.3}$ after hydrogen absorption, is consistent with both the gravimetric hydrogen storage capacity and the plateau pressures determined by the equilibrium and kinetic measurements that will be discussed in the next section.

Thermodynamics and kinetics of hydrogen sorption in Mg-Ni nanoparticles

Figure 5 shows the first hydrogen desorption and absorption cycle recorded at 150 °C on Mg-Ni NPs. Hydrogen desorption is initially fast but slows down significantly after about 1000 s, reaching completion in about 9000 s; hydrogen absorption is significantly faster, as usually reported for Mg-based systems [2]. The time dependence of the transformed fraction $\alpha(t)$ can be well described by Johnson-Mehl-Avrami-Kolmogorov (JMAK) nucleation and growth kinetics both for absorption and desorption [6]:

$$\alpha(t) = 1 - \exp[-(kt)^n] \quad (1)$$

where k is the rate constant and n the Avrami exponent linked to both geometrical features and rate-limiting factors of the growth. The details of the fit and the best-fit parameters are reported in Figure S3.

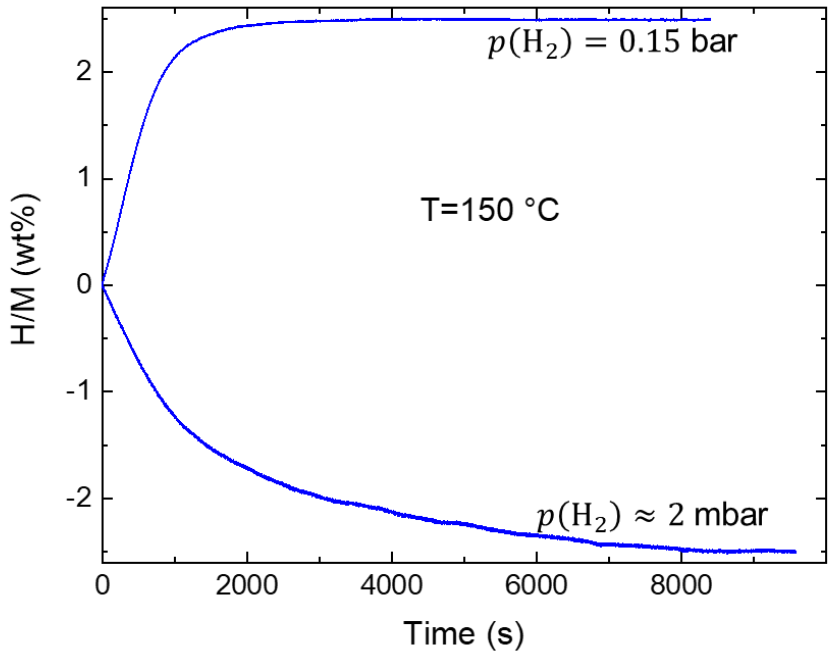

Figure 5. First hydrogen desorption and absorption kinetics recorded on Mg-Ni NPs (20 at.% Ni) at 150 °C.

The reversible gravimetric hydrogen capacity is about 2.5 wt%, much lower than what would be expected by assuming that both Mg and Mg_2Ni transform into the respective hydrides MgH_2 and Mg_2NiH_4. In fact, by considering a 20 at.% Ni content and assuming complete alloying of Ni into Mg_2Ni, the Mg ↔ MgH_2 reaction should contribute 2.45 wt% to the gravimetric capacity, while Mg_2Ni ↔ Mg_2NiH_4 should provide an additional 2.40 wt%, leading to a total 4.85 wt% for the nanocomposite sample. The measured 2.5 wt% capacity is consistent with the observation of $Mg_2NiH_{0.3}$, but not of Mg_2NiH_4, in the XRD profiles of hydrogenated NPs. This means that the transition to Mg_2NiH_4 does not occur under the present conditions of T and $p(H_2)$; therefore, Mg_2Ni contributes to the storage capacity exclusively through the transition to $Mg_2NiH_{0.3}$, which corresponds to only 0.18 wt% H for the overall composite. In summary, the missing formation of Mg_2NiH_4 is a heavy penalty to the storage capacity of Mg-Ni NPs, which remains well below the 4.2 wt% value recorded for Mg-Ti NPs with similar TM content (22 at.% Ti) [12].

In order to understand if Mg_2NiH_4 formation requires a higher driving force (i.e., higher $p(\mathrm{H}_2)$) and with the aim to characterize thermodynamic equilibrium in Mg-Ni NPs, we have recorded a pressure-composition isotherm (PCI) at 150 °C (Figure 6). The very steep initial part of the absorption branch ends at about 0.20 wt% H; considering that H solubility in Mg is very small, this must correspond to dissolution of H in Mg_2Ni, which is compatible with the formation of $Mg_2NiH_{0.3}$ suggested by XRD. A single sloping plateau characterizes both the absorption and the desorption branches of the PCI. The geometric average of the mid-plateau pressures (p_{abs} and p_{des} for absorption and desorption, respectively) is representative of the equilibrium pressure p_{eq}, from which the two branches deviate because of hysteresis. From the data in Figure 6, we calculate:

$$p_{eq} = (p_{abs} \cdot p_{des})^{1/2} \approx 7.5 \text{ mbar} \quad (2)$$

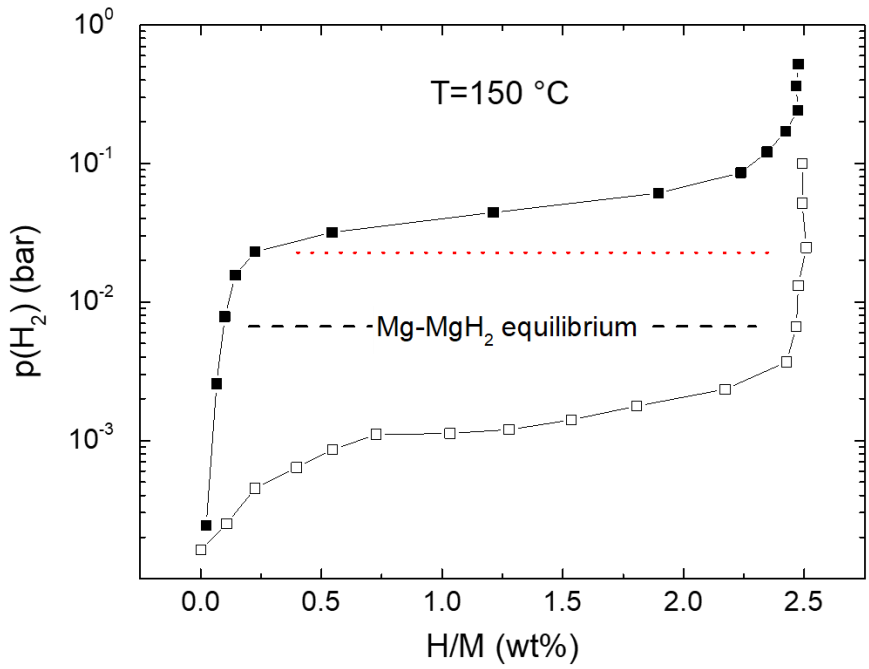

Figure 6. PCIs measured at 150 °C on the Mg-Ni NPs (20 at.% Ni) after the first hydrogen sorption cycle. The dashed black line marks the pressure expected for $Mg-MgH_2$ equilibrium; the red dotted line marks the expected pressure for $Mg_2Ni_{0.3} - Mg_2NiH_4$ equilibrium.

The equilibrium pressure obtained in this way for the Mg-Ni NPs is only slightly above the value $p_{eq} = 6.65 \text{ mbar}$ that can be calculated using the enthalpy and entropy of MgH_2 formation [7]. Moreover, the plateau width is very close to the value of 2.45 wt% H, which is calculated considering only the Mg ↔ MgH_2 transition (see above discussion for the kinetics). Therefore, we can safely conclude that the plateaus in the PCIs of Figure 6 correspond to the Mg ↔ MgH_2 transformation. The small increase of p_{eq} compared to bulk Mg may be due to nanoscale effects such as interface free energy and elastic stresses, as previously discussed for Mg-Ti composite NPs [13] and Mg@MgO core@shell NPs [40]. The hydrogen pressure expected for the $Mg_2NiH_{0.3} - Mg_2NiH_4$ equilibrium ($p_{eq} = 22.7 \text{ mbar}$) is about 3.4 times higher than for $Mg - MgH_2$ and is represented by the red dotted line in Figure 6. Therefore, a second absorption plateau should appear at pressures above the red-dotted line [41]. However, this is not observed up to $p(\mathrm{H}_2) \approx 0.7$ bar, the upper limit of our *in situ* set up.

The missing formation of Mg_2NiH_4 was reported also in Mg-Ni NPs (5 at.% Ni) encapsulated by reduced graphene oxide [27]; in that case, hydriding was carried out at 300 °C and $p(\mathrm{H}_2) = 15$ bar, which is about 5 times higher than the expected equilibrium pressure. Interestingly, Shao et al showed that an activation procedure at $p(\mathrm{H}_2) = 40$ bar and $T = 350$ °C was necessary for stoichiometric Mg_2Ni NPs with average size

of about 50 nm, after which full transformation into Mg_2NiH_4 could occur at $p(\mathrm{H_2}) \approx 6$ bar and $T = 300$ °C, with enthalpy and entropy of hydride formation quite close to those reported for bulk Mg_2NiH_4 [29]. Indeed, reports of full Mg_2NiH_4 formation in NPs typically involved T and $p(\mathrm{H_2})$ well above those used in the present experiments. For instance, stoichiometric Mg_2Ni NPs encapsulated in a partly hollow MgO shell and anchored on a graphene sheet turned into Mg_2NiH_4 at $p(\mathrm{H_2}) = 15$ bar and $T \approx 350$ °C [28]. Full hydriding of Mg_2Ni into Mg_2NiH_4 at $p(\mathrm{H_2}) = 70$ bar and $T = 300$ °C was reported in Mg-Ni NPs (4 at.% Ni) with size in the range of few hundred nm [42]. The mildest conditions we are aware of have been reported by Zlotea et al for ultra-small (≈ 4 nm) Mg-Ni NPs nanoconfined in mesoporous carbon, in which hydriding of Mg_2Ni to Mg_2NiH_4 was observed at $T = 210$ °C and $p(\mathrm{H_2}) = 5.7$ bar [30]. The initial formation of the reactive MgH_2-Mg_2NiH_4 composite was obtained starting from nanoconfined MgH_2 and Ni at about 300 °C under 20 bar of H_2.

Although it appears difficult to draw a systematic picture from an analysis of the available literature, the thermodynamic parameters measured by Shao et al after activation [29], as well as by Zlotea et al [30], suggest that the absence of Mg_2NiH_4 is not due to a change of the Mg_2Ni-Mg_2NiH_4 equilibrium in nanosized Mg-Ni systems, but rather to a kinetic limitation. This is consistent with the need of an activation procedure and/or a temperature in excess of 300 °C. Another possible factor is the Mg-Ni composition, as it appears that Mg_2NiH_4 formation is easier in stoichiometric Mg_2Ni rather than in MgH_2-Mg_2Ni two-phase material. This view is supported by a kinetic study of Mg-Mm-Ni alloys processed by ECAP, showing that the rate constants for the formation and decomposition of Mg_2NiH_4 at $T \approx 300$ °C are $50 - 150$ times lower than those for MgH_2 [21]. A similar difficulty in activating Mg-Mg_2Ni composites compared to stoichiometric Mg_2Ni was also reported in one of the first studies of ball-milled Mg-based hydrides [43]. It is therefore arguable that the formation of Mg_2NiH_4 may be completely kinetically hampered in the low $p(\mathrm{H_2}) - T$ regime of our interest.

At this point, it is interesting to draw a comparison between Mg-Ni, Mg-Ni-Fe, and Mg-Ti NPs in terms of both kinetics and thermodynamics. Figure S4 shows that the partial replacement of Ni with Fe, achieved by evaporating an equiatomic NiFe alloy instead of pure Ni, affects only moderately the PCI. A single sloping plateau with reversible gravimetric capacity of about 2.4 wt% H is observed also for Mg-Ni-Fe NPs. Therefore, also in this case the plateaus correspond to the Mg ↔ MgH_2 transformation and no further reactions involving Mg-Ni or Mg-Fe compounds occur at higher pressures. The two PCIs branches of Mg-Ni-Fe NPs are shifted upward compared to Mg-Ni NPs, indicating a moderate increase of the equilibrium pressure from ≈ 7.5 to ≈ 10.3 mbar. This slight destabilization may be the subject of future studies; however, the effect seems to be small and not exploitable to bring substantial changes to the $p(\mathrm{H_2}) - T$ conditions suitable for H_2 release. Figure S4 also reports the PCI of Mg-35 at.% Ti NPs [13] that display a similar reversible capacity of about 2.4 wt%. Although the equilibrium pressure of ≈ 7.1 mbar almost coincides with that of Mg-Ni NPs, Mg-Ti NPs exhibit flatter plateaus and significantly lower hysteresis; these features combined allow hydrogen release to take place at higher pressure in Mg-Ti NPs. However, for practical applications at $T = 150$ °C the desorption pressure lies in the range of a few mbar for both samples. The narrow plateau located at much lower pressure in Mg-Ti NPs was attributed to hydrogen in Ti-rich Mg-Ti metastable alloys, and is much less relevant for near-ambient applications [44].

The hydrogen sorption kinetics of Mg-Ni, Mg-Ni-Fe, and Mg-Ti NPs with a similar TM content are compared in Figure S5. The replacement of Ni with Fe has a moderate impact on the kinetics; the desorption rate seems to decrease a little, but the initial absorption rate is higher. Since these fine details also evolve with cycling as discussed below, we do not deem these changes very significant. On the contrary, Mg-Ti NPs (25 at.% Ti), besides reaching a significantly higher reversible capacity of about 3.9 wt%, as already noted, also exhibit remarkably faster reaction rates. The absorption time of about 200 s is particularly impressive, but also desorption is fast, being almost completed in 1000 s. This is attributed to the presence of small TiH_2 crystallites, which facilitate H_2 dissociation, enhance diffusion of atomic hydrogen along interfaces, and act as favourable sites for nucleation [13,45].

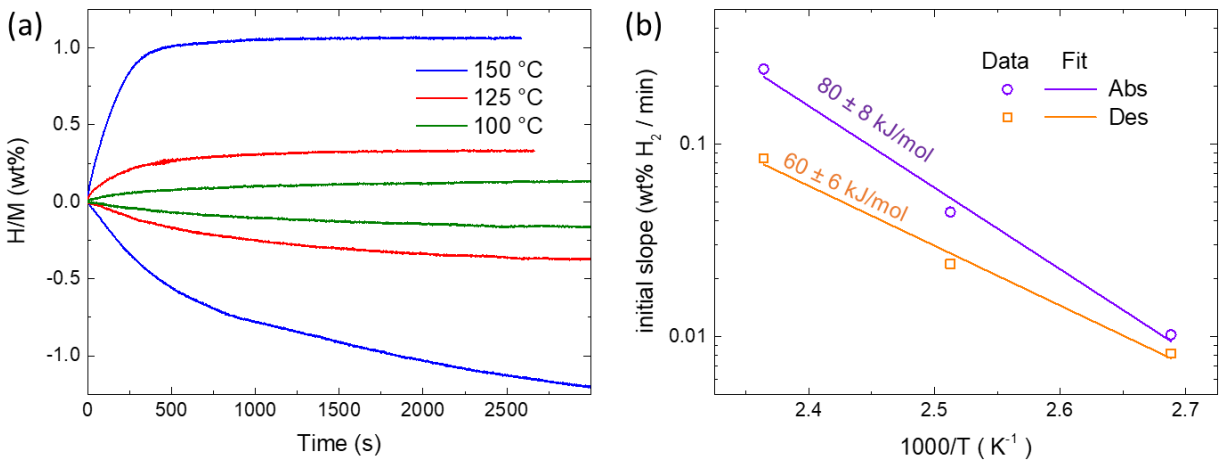

Figure 7. (a) Hydrogen sorption kinetics (3000 s desorption first, then absorption until saturation) of Mg-Ni NPs (20 at.% Ni) recorded at different temperatures (as indicated) after the PCIs reported in Figure 6. From the initial sorption rates in (a), an estimate of the initial activation energy is obtained from the Arrhenius plots in (b). Notice that the absorption pressure was tuned in order to maintain the driving force $p(\mathrm{H_2})/p_{eq}$ approximately constant; specifically, we used $p(\mathrm{H_2}) = 0.180, 0.047, \text{and } 0.011$ bar for $T = 150, 125, \text{and } 100$ °C, respectively. Desorption always started from high vacuum conditions.

In order to estimate the activation energy, we have measured hydrogen desorption and absorption kinetics at three different temperatures, i.e. 100, 125, and 150 °C (Figure 7a). Desorption (starting from the vacuum) turns out to be extremely sluggish at 100 °C and 125 °C. Moreover, the initial hydrogen release raises the pressure in the UHV chamber bringing it close to the equilibrium value, which is only 0.4 mbar and 1.8 mbar for Mg at $T = 100$ and 125 °C, respectively. This makes it impossible to record a full hydride-to-metal transformation at constant driving force (i.e., pressure). Therefore, instead of obtaining the rate constant from the fit of the full transformation using a specific kinetic model (as done in Figure S3), we consider the initial sorption rate, i.e. the slope of the linear incipit of the kinetics in Figure 7a. This approach is similar to the one proposed by Cho et al to determine the transformation dependence of the activation energy [27]. By reporting the initial slopes in the Arrhenius plot of Figure 7b, we can estimate the activation energies at the beginning of the transformation, obtaining $E_{abs} = 80 \pm 8$ kJ/mol and $E_{des} = 60 \pm 6$ kJ/mol for hydrogen absorption and desorption, respectively. The corresponding values for pure Mg span a wide range but are definitely higher, i.e. $E_{abs} = 95 - 130$ kJ/mol and $E_{des} = 120 - 160$ kJ/mol [6,7]. It is well known that the addition of transition metals and their oxides [46] or hydrides [47] can significantly lower the activation energies by favouring H_2 dissociation/recombination, H diffusion, and heterogeneous nucleation [48]. Our value of E_{des} is close to that reported for Ni-doped Mg NPs on graphene (64.7 kJ/mol, [49]) and for ball-milled MgH_2 with either TiH_2 (58.4 kJ/mol, [50]) or Nb_2O_5 (62 kJ/mol, [51]) additives, which are a sort of benchmark for catalysed H_2 desorption from MgH_2. Smaller E_{des} values and faster desorption kinetics at low T were reported for the already discussed Mg-Ti NPs (35 kJ/mol, [12]) and for ultra-small Mg NPs (3.4 nm) embedded in Ni-doped activated carbon (43 kJ/mol, [52]). Notice that Mg-Ti NPs have also a lower $E_{abs} = 52$ kJ/mol [12], consistent with the extremely fast hydrogen absorption kinetics displayed in Figure S5. A summarizing table of the activation energies measured in Mg-based nanostructures for hydrogen storage can be found in a recent review [48].

Finally, we comment on the stability of the hydrogen sorption kinetics upon cycling. Figure S6 shows that the amount of hydrogen released after 3000s in the third sorption cycle is about 1.2 wt%, significantly lower than 1.7 wt% recorded in the very first cycle (see Figure 5). This figure drops further to about 0.75 wt% in the 8th cycle, then it seems to stabilize, reaching about 0.68 wt% in the 11th cycle. The re-absorbed amount corresponds reasonably well to the released one. For comparison, the cycling stability of Mg-Ti NPs is also shown in Figure S6. There are two main causes for the degrading kinetics of Mg-based NPs with cycling. The first one is the coarsening of the nanostructure, which is particularly evident by comparing panels (a) and (b) in Figure 1. The formation of larger aggregates implies that hydrogen must diffuse over longer distances in

order to complete the transformation. Moreover, in the present case the increasing segregation between Mg and Mg_2Ni may leave large Mg/MgH_2 volumes depleted of Mg_2Ni, the catalytic action of which is necessary for the dissociation/recombination of the H_2 molecule. This problem is intrinsically linked to the instability of nanostructures. The second cause is a possible decline of the surface reactivity due to contamination by residual impurities within the hydrogen gas. The formation of MgO surface layers is not only detrimental to the kinetics but also reduces the overall gravimetric capacity. This issue may be solved at the laboratory scale by adopting gas purifiers, however the devised hydrogen purity in real-world applications cannot be tremendously high (typically 99.97 %, i.e. ≈ 10 times worse than in present experiments). In this respect, the use of carbon nanostructures as wrapping layers with selective permeation for hydrogen is a promising strategy to improve the kinetic stability, because both coarsening and surface contamination may be significantly suppressed [27,52,53].

Conclusions

Bi-elemental Mg-Ni NPs can be successfully prepared by gas phase condensation in a He/H_2 atmosphere using two independent thermal vapour sources. The intermetallic compound Mg_2Ni forms readily by heating the NPs to 150 °C under vacuum. The exposure to a mild $p(\mathrm{H_2}) = 0.15$ bar at 150 °C leads to the formation of a MgH_2-$Mg_2NiH_{0.3}$ nanocomposite, the hydrogen sorption kinetics of which at 150 °C are remarkable, although not as fast as previously reported for Mg-Ti NPs.

The fundamental difference between the present Mg-Ni NPs and the previously studied Mg-Ti NPs is the ability of Ni to form an alloy with Mg, while Mg and Ti are immiscible. Moreover, TiH_2 is very stable and does not dissociate at the typical $p(\mathrm{H_2}), T$ conditions used for reversible hydrogen storage, while Mg_2Ni is expected to form Mg_2NiH_4, which is less stable than MgH_2. Since the equilibrium pressure of Mg_2NiH_4 is higher than MgH_2, a synergistic coupling at the nanoscale mediated by elastic stresses could lead to a destabilization of MgH_2, making it possible to release hydrogen at higher pressure. Moreover, given that two H atoms are available for the reversible process per each Mg atom, the maximum storage capacity for Mg-Ti and Mg-Ni NPs should be the same if the weight fraction of the *3d* TM is kept constant. Unfortunately, the transformation from Mg_2Ni to Mg_2NiH_4 is not observed at 150 °C in the Mg-Ni NPs, even at $p(\mathrm{H_2})$ well above the expected equilibrium threshold, revealing a stronger kinetic barrier against hydride formation in the intermetallic Mg_2Ni compared to Mg. As a result, the Mg-Ni NPs exhibit a gravimetric storage capacity of only 2.5 wt%, falling short of the 4.9 wt% value that would be expected for a Mg-Mg_2Ni composite at 20 at.% Ni where the two phases should contribute similarly to reversible hydrogen storage. This represents a strong limitation to the use of Mg-Ni NPs in the low temperature regime. The equilibrium pressure, determined from the pressure-composition isotherm at 150 °C, is only slightly higher than expected for the bulk Mg-MgH_2 system and very close to the one measured for Mg-35 at.%Ti NPs.

The decrease of the hydrogen desorption rates upon cycling is linked to the coarsening of the NPs aggregates and to the segregation of Mg and Mg_2Ni phases. Differently, in the case of Mg-Ti NPs, TiH_2 small crystallites remain finely dispersed within Mg, ensuring the necessary catalytic activity for H_2 dissociation/recombination and providing preferential paths for diffusion as well as nucleation sites. These features, combined with a grain refining action of the dispersed TiH_2 phase, confer a higher stability upon cycling, although some degradation of the kinetic performance is intimately linked to the metastable nature of nanostructures.

In summary, the comparison between Mg-Ni and Mg-Ti NPs highlights a number of microstructural differences that have strong impact on their hydrogen sorption kinetics, and contributes to a deeper understanding of Mg-based nanocomposites for hydrogen storage. Because of the missing Mg_2NiH_4 formation in the low temperature regime, Mg-Ni NPs fall short of both gravimetric hydrogen capacity and hydrogen sorption rates of Mg-Ti NPs, while displaying the same equilibrium pressure.

References

[1] M. Hirscher, V.A. Yartys, M. Baricco, J. Bellosta von Colbe, D. Blanchard, R.C. Bowman, D.P. Broom, C.E. Buckley, F. Chang, P. Chen, Y.W. Cho, J.C. Crivello, F. Cuevas, W.I.F. David, P.E. de Jongh, R. V.

Denys, M. Dornheim, M. Felderhoff, Y. Filinchuk, G.E. Froudakis, D.M. Grant, E.M.A. Gray, B.C. Hauback, T. He, T.D. Humphries, T.R. Jensen, S. Kim, Y. Kojima, M. Latroche, H.W. Li, M. V. Lototskyy, J.W. Makepeace, K.T. Møller, L. Naheed, P. Ngene, D. Noréus, M.M. Nygård, S. ichi Orimo, M. Paskevicius, L. Pasquini, D.B. Ravnsbæk, M. Veronica Sofianos, T.J. Udovic, T. Vegge, G.S. Walker, C.J. Webb, C. Weidenthaler, C. Zlotea, Materials for hydrogen-based energy storage – past, recent progress and future outlook, J. Alloys Compd. 827 (2020) 153548. doi:10.1016/j.jallcom.2019.153548.

[2] V.A. Yartys, M.V. Lototskyy, E. Akiba, R. Albert, V.E. Antonov, J.R. Ares, M. Baricco, N. Bourgeois, C.E. Buckley, J.M. Bellosta von Colbe, J.-C. Crivello, F. Cuevas, R.V. Denys, M. Dornheim, M. Felderhoff, D.M. Grant, B.C. Hauback, T.D. Humphries, I. Jacob, T.R. Jensen, P.E. de Jongh, J.-M. Joubert, M.A. Kuzovnikov, M. Latroche, M. Paskevicius, L. Pasquini, L. Popilevsky, V.M. Skripnyuk, E. Rabkin, M.V. Sofianos, A. Stuart, G. Walker, H. Wang, C.J. Webb, M. Zhu, Magnesium based materials for hydrogen based energy storage: Past, present and future, Int. J. Hydrogen Energy. 44 (2019). doi:10.1016/j.ijhydene.2018.12.212.

[3] J.-C. Crivello, B. Dam, R. V. Denys, M. Dornheim, D.M. Grant, J. Huot, T.R. Jensen, P. de Jongh, M. Latroche, C. Milanese, D. Milčius, G.S. Walker, C.J. Webb, C. Zlotea, V.A. Yartys, Review of magnesium hydride-based materials: development and optimisation, Appl. Phys. A. 122 (2016) 97. doi:10.1007/s00339-016-9602-0.

[4] J.-C. Crivello, R. V. Denys, M. Dornheim, M. Felderhoff, D.M. Grant, J. Huot, T.R. Jensen, P. de Jongh, M. Latroche, G.S. Walker, C.J. Webb, V.A. Yartys, Mg-based compounds for hydrogen and energy storage, Appl. Phys. A. 122 (2016) 85. doi:10.1007/s00339-016-9601-1.

[5] R. Hardian, C. Pistidda, A.-L. Chaudhary, G. Capurso, G. Gizer, H. Cao, C. Milanese, A. Girella, A. Santoru, D. Yigit, H. Dieringa, K.U. Kainer, T. Klassen, M. Dornheim, Waste Mg-Al based alloys for hydrogen storage, Int. J. Hydrogen Energy. 43 (2018) 16738–16748. doi:https://doi.org/10.1016/j.ijhydene.2017.12.014.

[6] J.F. Fernández, C.R. Sánchez, Rate determining step in the absorption and desorption of hydrogen by magnesium, J. Alloys Compd. 340 (2002) 189–198. doi:10.1016/S0925-8388(02)00120-2.

[7] M. Paskevicius, D.A. Sheppard, C.E. Buckley, Thermodynamic Changes in Mechanochemically Synthesized Magnesium Hydride Nanoparticles, J. Am. Chem. Soc. 6 (2010) 469–472. doi:10.1021/ja908398u.

[8] J. Huot, F. Cuevas, S. Deledda, K. Edalati, Y. Filinchuk, T. Grosdidier, B.C. Hauback, M. Heere, T.R. Jensen, M. Latroche, S. Sartori, Mechanochemistry of Metal Hydrides: Recent Advances, Materials (Basel). 12 (2019) 2778. doi:10.3390/ma12172778.

[9] L. Pasquini, The effects of nanostructure on the hydrogen sorption properties of magnesium-based metallic compounds: A review, Crystals. 8 (2018). doi:10.3390/cryst8020106.

[10] C.J. Webb, A review of catalyst-enhanced magnesium hydride as a hydrogen storage material, J. Phys. Chem. Solids. 84 (2015). doi:10.1016/j.jpcs.2014.06.014.

[11] K. Sivula, R. van de Krol, Semiconducting materials for photoelectrochemical energy conversion, Nat. Rev. Mater. 2016 12. 1 (2016) 1–16. doi:10.1038/natrevmats.2015.10.

[12] N. Patelli, A. Migliori, L. Pasquini, Reversible Metal-Hydride Transformation in Mg-Ti-H Nanoparticles at Remarkably Low Temperatures, ChemPhysChem. 20 (2019) 1325–1333. doi:10.1002/cphc.201801186.

[13] N. Patelli, A. Migliori, V. Morandi, L. Pasquini, Interfaces within biphasic nanoparticles give a boost to magnesium-based hydrogen storage, Nano Energy. 20 (2020) 1325–1333. doi:10.1002/cphc.201801186.

[14] S.-I. Orimo, H. Fujii, Materials science of Mg-Ni-based new hydrides, Appl. Phys. A. 72 (2001) 167–186. doi:10.1007/s003390100771.

[15] K. Zeng, T. Klassen, W. Oelerich, R. Bormann, Thermodynamic analysis of the hydriding process of Mg–Ni alloys, J. Alloys Compd. 283 (1999) 213–224. doi:10.1016/S0925-8388(98)00902-5.

[16] J.J. Reilly, R.H. Wiswall, The Reaction of Hydrogen with Alloys of Magnesium and Nickel and the Formation of Mg2NiH4, Inorg. Chem. 7 (1968) 2254–2256. http://pubs.acs.org/doi/pdf/10.1021/ic50069a016 (accessed January 23, 2018).

[17] J. Huot, G. Liang, R. Schulz, Mechanically alloyed metal hydride systems, Appl. Phys. A Mater. Sci. Process. 72 (2001) 187–195. doi:10.1007/s003390100772.

[18] G. Liang, J. Huot, S. Boily, A. Van Neste, R. Schulz, Catalytic effect of transition metals on hydrogen sorption in nanocrystalline ball milled MgH2–Tm (Tm=Ti, V, Mn, Fe and Ni) systems, J. Alloys Compd. 292 (1999) 247–252. doi:10.1016/S0925-8388(99)00442-9.

[19] J. Huot, D.B. Ravnsbæk, J. Zhang, F. Cuevas, M. Latroche, T.R. Jensen, Mechanochemical synthesis of hydrogen storage materials, Prog. Mater. Sci. 58 (2013) 30–75. doi:10.1016/j.pmatsci.2012.07.001.

[20] V. Skripnyuk, E. Buchman, E. Rabkin, Y. Estrin, M. Popov, S. Jorgensen, The effect of equal channel angular pressing on hydrogen storage properties of a eutectic Mg–Ni alloy, J. Alloys Compd. 436 (2007) 99–106. doi:10.1016/J.JALLCOM.2006.07.030.

[21] S. Løken, J.K. Solberg, J.P. Maehlen, R. V. Denys, M. V. Lototsky, B.P. Tarasov, V.A. Yartys, Nanostructured Mg–Mm–Ni hydrogen storage alloy: Structure–properties relationship, J. Alloys Compd. 446–447 (2007) 114–120. doi:10.1016/J.JALLCOM.2006.11.200.

[22] A. Révész, Z. Kánya, T. Verebélyi, P.J. Szabó, A.P. Zhilyaev, T. Spassov, The effect of high-pressure torsion on the microstructure and hydrogen absorption kinetics of ball-milled Mg70Ni30, J. Alloys Compd. 504 (2010) 83–88. doi:10.1016/j.jallcom.2010.05.058.

[23] Á. Révész, M. Gajdics, E. Schafler, M. Calizzi, L. Pasquini, Dehydrogenation-hydrogenation characteristics of nanocrystalline Mg2Ni powders compacted by high-pressure torsion, J. Alloys Compd. 702 (2017) 84–91. doi:10.1016/j.jallcom.2017.01.261.

[24] P. De Rango, J. Wen, N. Skryabina, L. Laversenne, D. Fruchart, M. Borges, Hydrogen storage properties of Mg-Ni alloys processed by fast forging, Energies. 13 (2020). doi:10.3390/en13133509.

[25] J.O. Fadonougbo, H.J. Kim, B.C. Suh, J.Y. Suh, Y.S. Lee, J.H. Shim, C.D. Yim, Y.W. Cho, Kinetics and thermodynamics of near eutectic Mg-Mg2Ni composites produced by casting process, Int. J. Hydrogen Energy. 45 (2020) 29009–29022. doi:10.1016/J.IJHYDENE.2020.07.181.

[26] Y. Wu, M. V. Lototsky, J.K. Solberg, V.A. Yartys, Microstructural evolution and improved hydrogenation–dehydrogenation kinetics of nanostructured melt-spun Mg–Ni–Mm alloys, J. Alloys Compd. 509 (2011) S640–S645. doi:10.1016/J.JALLCOM.2010.11.140.

[27] E.S. Cho, A.M. Ruminski, Y.-S. Liu, P.T. Shea, S. Kang, E.W. Zaia, J.Y. Park, Y.-D. Chuang, J.M. Yuk, X. Zhou, T.W. Heo, J. Guo, B.C. Wood, J.J. Urban, Hierarchically Controlled Inside-Out Doping of Mg Nanocomposites for Moderate Temperature Hydrogen Storage, Adv. Funct. Mater. 27 (2017) 1704316. doi:10.1002/ADFM.201704316.

[28] J. Zhang, Y. Zhu, H. Lin, Y. Liu, Y. Zhang, S. Li, Z. Ma, L. Li, Metal Hydride Nanoparticles with Ultrahigh Structural Stability and Hydrogen Storage Activity Derived from Microencapsulated Nanoconfinement, Adv. Mater. 29 (2017) 1700760. doi:10.1002/adma.201700760.

[29] H. Shao, H. Xu, Y. Wang, X. Li, Preparation and hydrogen storage properties ofMg2Ni intermetallic nanoparticles, Nanotechnology. 15 (2003) 269. doi:10.1088/0957-4484/15/3/006.

[30] C. Zlotea, F. Cuevas, J. Andrieux, C. Matei Ghimbeu, E. Leroy, E. Léonel, S. Sengmany, C. Vix-Guterl, R. Gadiou, T. Martens, M. Latroche, Tunable synthesis of (Mg-Ni)-based hydrides nanoconfined in templated carbon studied by in situ synchrotron diffraction, Nano Energy. 2 (2013) 12–20. doi:10.1016/j.nanoen.2012.07.005.

[31] M. Malekzadeh, M.T. Swihart, Vapor-phase production of nanomaterials, Chem. Soc. Rev. 50 (2021) 7132–7249. doi:10.1039/d0cs01212b.

[32] G. Ischia, H.-R. Wenk, L. Lutterotti, F. Berberich, Quantitative Rietveld texture analysis of zirconium from single synchrotron diffraction images, J. Appl. Crystallogr. 38 (2005) 377–380. doi:10.1107/S0021889805006059.

[33] C.G. Granqvist, R.A. Buhrman, Ultrafine metal particles, J. Appl. Phys. 47 (1976) 2200–2219. doi:10.1063/1.326081.

[34] L. Pasquini, E. Callini, E. Piscopiello, A. Montone, M.V. Antisari, E. Bonetti, Metal-hydride transformation kinetics in Mg nanoparticles, Appl. Phys. Lett. 94 (2009) 041918. doi:10.1063/1.3077186.

[35] M. Calizzi, D. Chericoni, L.H. Jepsen, T.R. Jensen, L. Pasquini, Mg-Ti nanoparticles with superior kinetics for hydrogen storage, Int. J. Hydrogen Energy. 41 (2016) 14447–14454. doi:10.1016/j.ijhydene.2016.03.071.

[36] N. Patelli, M. Calizzi, A. Migliori, V. Morandi, L. Pasquini, Hydrogen Desorption Below 150 °C in MgH_2 –TiH_2 Composite Nanoparticles: Equilibrium and Kinetic Properties, J. Phys. Chem. C. 121 (2017) 11166–11177. doi:10.1021/acs.jpcc.7b03169.

[37] A. Surrey, K. Nielsch, B. Rellinghaus, Comments on ”Evidence of the hydrogen release mechanism in bulk MgH2”, Sci. Rep. 7 (2017) 44216. doi:10.1038/srep44216.

[38] N. Lobo, A. Takasaki, K. Mineo, A. Klimkowicz, K. Goc, Stability investigation of the γ-MgH2 phase synthesized by high-energy ball milling, Int. J. Hydrogen Energy. 44 (2019) 29179–29188. doi:10.1016/J.IJHYDENE.2019.02.191.

[39] L. Pasquini, E. Callini, M. Brighi, F. Boscherini, A. Montone, T.R. Jensen, C. Maurizio, M.V. Antisari, E. Bonetti, Magnesium nanoparticles with transition metal decoration for hydrogen storage, J. Nanoparticle Res. 13 (2011). doi:10.1007/s11051-011-0509-6.

[40] L. Pasquini, M. Sacchi, M. Brighi, C. Boelsma, S. Bals, T. Perkisas, B. Dam, Hydride destabilization in core-shell nanoparticles, Int. J. Hydrogen Energy. 39 (2014) 2115–2123. doi:10.1016/j.ijhydene.2013.11.085.

[41] A.A. Volodin, R. V Denys, C. Wan, I.D. Wijayanti, Suwarno, B.P. Tarasov, V.E. Antonov, V.A. Yartys, Study of hydrogen storage and electrochemical properties of AB2-type Ti0.15Zr0.85La0.03Ni1.2Mn0.7V0.12Fe0.12 alloy, J. Alloys Compd. 793 (2019) 564–575. doi:https://doi.org/10.1016/j.jallcom.2019.03.134.

[42] E. Callini, L. Pasquini, T.R. Jensen, E. Bonetti, Hydrogen storage properties of Mg-Ni nanoparticles, Int. J. Hydrogen Energy. 38 (2013). doi:10.1016/j.ijhydene.2013.05.139.

[43] G. Liang, S. Boily, J. Huot, A. Van Neste, R. Schulz, Mechanical alloying and hydrogen absorption properties of the Mg–Ni system, J. Alloys Compd. 267 (1998) 302–306. doi:10.1016/S0925-8388(97)00533-1.

[44] D.M. Borsa, R. Gremaud, A. Baldi, H. Schreuders, J.H. Rector, B. Kooi, P. Vermeulen, P.H.L. Notten, B. Dam, R. Griessen, Structural, optical, and electrical properties of Mgy Ti1-y Hx thin films, Phys. Rev. B - Condens. Matter Mater. Phys. 75 (2007) 1–9. doi:10.1103/PhysRevB.75.205408.

[45] X. Duan, R. Griessen, R.J. Wijngaarden, S. Kamin, N. Liu, Self-recording and manipulation of fast long-

range hydrogen diffusion in quasifree magnesium, Phys. Rev. Mater. 2 (2018) 085802. doi:10.1103/PhysRevMaterials.2.085802.

[46] M. Dornheim, S. Doppiu, G. Barkhordarian, U. Boesenberg, T. Klassen, O. Gutfleisch, R. Bormann, Hydrogen storage in magnesium-based hydrides and hydride composites, Scr. Mater. 56 (2007) 841–846. doi:10.1016/j.scriptamat.2007.01.003.

[47] P. Rizo-Acosta, F. Cuevas, M. Latroche, Hydrides of early transition metals as catalysts and grain growth inhibitors for enhanced reversible hydrogen storage in nanostructured magnesium, J. Mater. Chem. A. 7 (2019) 23064–23075. doi:10.1039/C9TA05440E.

[48] L. Pasquini, Design of Nanomaterials for Hydrogen Storage, Energies. 13 (2020) 3503. doi:10.3390/en13133503.

[49] G. Xia, Y. Tan, X. Chen, D. Sun, Z. Guo, H. Liu, L. Ouyang, M. Zhu, X. Yu, Monodisperse Magnesium Hydride Nanoparticles Uniformly Self-Assembled on Graphene, Adv. Mater. 27 (2015) 5981–5988. doi:10.1002/adma.201502005.

[50] J. Lu, Y.J. Choi, Z.Z. Fang, H.Y. Sohn, E. Rönnebro, Hydrogen Storage Properties of Nanosized MgH2-0.1TiH2 Prepared by Ultrahigh-Energy - High-Pressure Milling, J. Am. Chem. Soc. 131 (2009) 15843–15852.

[51] G. Barkhordarian, T. Klassen, R. Bormann, Kinetic investigation of the effect of milling time on the hydrogen sorption reaction of magnesium catalyzed with different Nb2O 5 contents, J. Alloys Compd. 407 (2006) 249–255. doi:10.1016/j.jallcom.2005.05.037.

[52] S.S. Shinde, D.H. Kim, J.Y. Yu, J.H. Lee, Self-assembled air-stable magnesium hydride embedded in 3-D activated carbon for reversible hydrogen storage, Nanoscale. 9 (2017) 7094–7103. doi:10.1039/c7nr01699a.

[53] E.S. Cho, A.M. Ruminski, S. Aloni, Y.-S. Liu, J. Guo, J.J. Urban, Graphene oxide/metal nanocrystal multilaminates as the atomic limit for safe and selective hydrogen storage, Nat. Commun. 7 (2016) 10804. doi:10.1038/ncomms10804.